ECS Journal of Solid State
Science and Technology

Influence of Ring Contraction on the Electronic Structure of Nickel Tetrapyrrole Complexes: Corrole vs Porphyrin

ECS Journal of Solid State Science and Technology, 2020 **9** 061005

Influence of Ring Contraction on the Electronic Structure of Nickel Tetrapyrrole Complexes: Corrole vs Porphyrin

Jan Herritsch,[1] Jan-Niclas Luy,[1] Sebastian Rohlf,[2,3] Manuel Gruber,[2] Benedikt P. Klein,[1] Matthias Kalläne,[2,3] Peter Schweyen,[4] Martin Bröring,[4] Kai Rossnagel,[2,5] Ralf Tonner,[1,a] and J. Michael Gottfried[1,z]

[1]*Fachbereich Chemie, Philipps-Universität Marburg, 35032 Marburg, Germany*
[2]*Institut für Experimentelle und Angewandte Physik, Christian-Albrechts-Universität zu Kiel, 24098 Kiel, Germany*
[3]*Ruprecht-Haensel-Labor, Christian-Albrechts-Universität zu Kiel, 24098 Kiel, Germany*
[4]*Institut für Anorganische und Analytische Chemie, Technische Universität Braunschweig, 38106 Braunschweig, Germany*
[5]*Ruprecht-Haensel-Labor, Deutsches Elektronen-Synchrotron DESY, 22607 Hamburg, Germany*

The influence of the contracted corrole macrocycle, in comparison to the larger porphyrin macrocycle, on the electronic structure of nickel was studied with X-ray and ultraviolet photoelectron spectroscopy (XPS, UPS) and near-edge X-ray absorption fine structure (NEXAFS) spectroscopy. Synthesis and in situ characterization of the Ni complexes of octaethylporphyrin (NiOEP) and hexaethyldimethylcorrole (NiHEDMC) were performed in ultra-high vacuum. XPS and NEXAFS spectra reveal a +2 oxidation state and a low-spin d^8 electron configuration of Ni in both complexes, despite the formal trianionic nature of the corrole ligand. UPS, in combination with density functional theory (DFT) calculations, support the electronic structure of a Ni(II) corrole with a π-radical character of the ligand. The NEXAFS spectra also reveal differences in the valence electronic structure, which are attributed to the size mismatch between the small Ni(II) center and the larger central cavity of NiOEP. Analysis of the gas-phase structures shows that the Ni−N bonds in NiOEP are 4%–6% longer than those in NiHEDMC, even when NiOEP adopts a ruffled conformation. The individual interactions that constitute the Ni−ligand bond are altogether stronger in the corrole complex, according to bonding analysis within the energy decomposition analysis and the natural orbitals for chemical valence theory (EDA-NOCV).

 [DOI: 10.1149/2162-8777/ab9e18]

Manuscript received May 31, 2020. Published July 8, 2020. *This paper is part of the JSS Focus Issue on Porphyrins, Phthalocyanines, and Supramolecular Assemblies in Honor of Karl M. Kadish.*

Supplementary material for this article is available online

Nickel complexes of porphyrins and related tetrapyrrolic macrocycles play a prominent role in nature as the active centers of enzymes,[1] such as the cofactor F430 found in methanogenic archaea, and occur as biomarkers in sediments.[2,3] Their coordination chemistry[4–7] is of broad scientific and technological interest, especially in connection with potential applications as molecular sensors and switches.[8–10] The porphyrin ligand provides a square-planar coordination environment for the central nickel ion, which normally has a low-spin d^8 electron configuration. However, nickel porphyrin complexes tend to undergo out-of-plane distortion leading to ruffled conformations that were observed in crystal structures and in solution for different porphyrin ligands.[11–18] This tendency for distortion can be explained by the size mismatch between the small nickel(II) center and the larger central cavity of the ligand macrocycle. The ruffled conformation leads to an effective contraction of the macrocycle and thus to a more favorable coordination geometry for the small low-spin Ni(II) cation.[14,19] Additional axial coordination used to manipulate the spin state of the nickel center can be accompanied by a change of the conformation of the porphyrin.[20]

A contracted coordination environment for the central nickel(II) cation can also be achieved through modification of the ligand skeletal structure, i.e., by replacing the porphyrin by the related corrole.[21–24] The corrole contains one carbon atom less in the macrocycle and thus can be described as a ring-contracted porphyrin (Fig. 1a). Its molecular structure with a missing methine (=CH−) bridge leads to a modified electronic structure. In accordance with the rules of aromaticity, corroles comprise three NH-groups and therefore are formally trianionic ligands.[22] Their smaller ring with the contracted cavity provides a tighter coordination environment,[23] making corroles promising ligands for the stabilization of small metal ions in high oxidation states.[25]

In contrast to nickel porphyrin complexes, nickel corrole complexes have received only little attention in the past, despite their interesting electronic structure.[23] In the early days of corrole research, nickel corroles were synthesized and described as paramagnetic, non-aromatic compounds.[26–29] However, at that time the exact structure of nickel corroles was unclear. The structure was assumed as a peculiar, not fully conjugated macrocycle with an additional hydrogen atom at one of the *meso*-methine bridges.[26,27] This sp^3 center would interrupt the conjugation path along the macrocycles and thus destroy the aromatic character. An alternative description of the ground-state of nickel corroles as a nickel(II) d^8 central atom with a π-radical ligand system did not follow until much later and was supported by electron paramagnetic resonance (EPR) spectroscopy and crystallographic structure analysis.[30] This interpretation was later confirmed by DFT calculations.[23,31,32]

In the present paper, a nickel corrole complex is—to our knowledge—for the first time characterized by X-ray photoelectron spectroscopy (XPS) and near-edge X-ray absorption fine structure (NEXAFS) spectroscopy under ultra-high vacuum (UHV) conditions. By this approach, the oxidation state of the central atom is verified and the corrole complex is compared to a related nickel porphyrin to reveal changes in the electronic structure induced by a porphyrinoid ring contraction.

Until now, most studies of nickel corrole complexes have been performed with octaalkyl substituted ligands. Therefore, the 2,3,8,12,17,18-hexaethyl-7-13-dimethylcorrole (H_3HEDMC) ligand provides a good starting point for the investigation of nickel corroles under UHV conditions. 2,3,7,8,12,13,17,18-octaethylporphyrin (H_2OEP) was used as the porphyrin reference system. The studied complexes were obtained by direct metalation achieved by physical vapor deposition (PVD) of nickel onto thin films of H_3HEDMC and H_2OEP, respectively, in UHV. This previously established method[33–41] for the

[a]Present address: Institut für Physikalische und Theoretische Chemie, Universität Regensburg, 93053 Regensburg, Germany.
[z]E-mail: michael.gottfried@chemie.uni-marburg.de

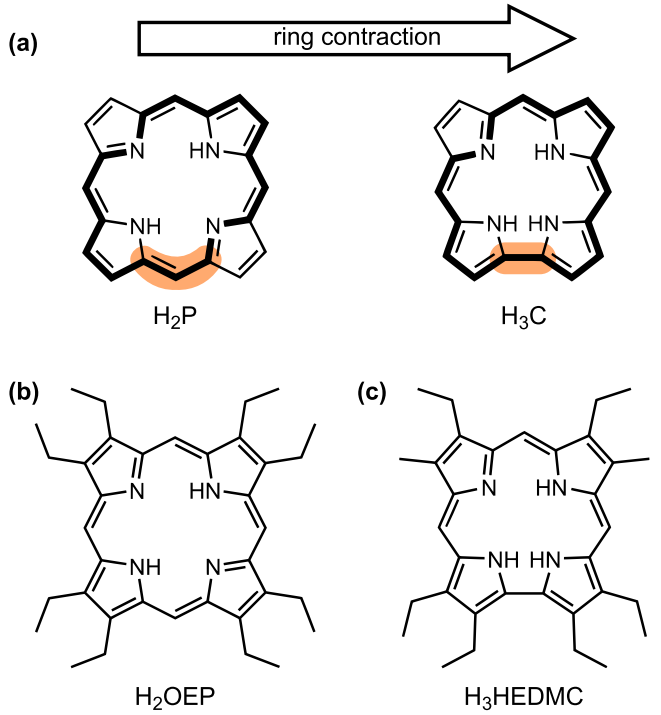

Figure 1. Molecular structures of (a) the free-base porphine and corrole macrocycles, (b) 2,3,7,8,12,13,17,18-octaethylporphyrin (H_2OEP) and (c) 2,3,8,12,17,18-hexaethyl-7-13-dimethylcorrole (H_3HEDMC). The structural difference regarding the methine bridge is highlighted and the aromatic 18π electron delocalization pathway is shown by bold lines.

preparation of transition-metal tetrapyrrole complexes has the formidable advantage of providing exceptionally clean UHV conditions during the metalation and immediately following in situ spectroscopic characterization of the complexes. As a result, influences of oxidation or other reactions with ambient gases are avoided, which is especially important when surface spectroscopic techniques such as XPS are employed. The thin films of the free corrole and porphyrin bases were also prepared in UHV by PVD of the respective molecules onto a Ag (111) single crystal surface. This in situ metalation was previously successfully applied for the metalation of H_2OEP and H_3HEDMC with iron.[34] The direct metalation with nickel was established for different tetrapyrrole ligand systems and provides the basis for our study.[40,42–44] Here, we apply conditions of Ni deficiency (i.e., an excess of ligand molecules) to minimize the amount of remaining unreacted Ni. The limited diffusion and reaction depth of transition metal atoms in the molecular thin films ensures that only the topmost layers of the thin films are metalated.[45] The complexes are therefore electronically decoupled from the Ag surface by layers of pristine, unmetalated molecules.[46]

Using XPS, UPS, NEXAFS, and DFT calculations, we show that NiOEP and NiHEDMC both exhibit a nickel(II) central atom in a low-spin d^8 electron configuration. Hence, our results support the description of the corrole ligand in NiHEDMC as a π-radical. With DFT, we analyze differences in the geometric and electronic structures between the corrole and porphyrin complexes. By using the energy decomposition analysis combined with the natural orbitals for chemical valence theory (EDA-NOCV), we characterize the individual bonding interactions between ligand and central atom.

Experimental and Computational Details

H_3HEDMC was prepared according to the reported procedure.[34] H_2OEP (purity > 98%, J&K Scientific Ltd) and its nickel complex NiOEP (purity > 95%, Por-Lab, Porphyrin Laboratories GmbH) were purchased from commercial sources. All experiments were performed in UHV with a base pressure below 10^{-9} mbar. Note that the UHV conditions ensure that the oxygen and water partial pressures during the preparation and characterization are at least 10^6 times lower than under typical glove box conditions. The Ag (111) single crystal used as substrate was cleaned by repeated cycles of Ar^+ ion bombardment (0.5 keV) followed by annealing (800 K). Surface cleanliness was checked prior to the experiments by XPS. H_3HEDMC, H_2OEP and NiOEP were vapor-deposited onto the Ag(111) surface from a Knudsen cell evaporator held at 195, 220 and 250 °C, respectively. The flux was monitored at the sample position using a quartz crystal microbalance and the thickness of the resulting thin films was in the range of 10 monolayers. Metalation was performed by vapor deposition of nickel onto the organic multilayers using electron beam evaporators (FOCUS EFM-3/4). Substoichiometric amounts of Ni were used to avoid or minimize the presence of unreacted Ni(0), as was subsequently confirmed by spectroscopy. During the preparation, the Ag sample was kept at room temperature. For XPS, a monochromated Al K_α X-ray source (1486.7 eV) and a SPECS Phoibos 150 electron energy analyzer equipped with an MCD-9 multichanneltron detector were used. A linear background was subtracted from the Ni 2p spectra. Valence photoemission spectra (UPS) were measured with the same analyzer and a gas-discharge UV source providing He-I radiation (21.2 eV). Near-edge X-ray absorption fine structure (NEXAFS) spectroscopy was performed at the ASPHERE experimental station at the beamline P04[47] of PETRA III (DESY, Hamburg). Several spectra were collected in total electron yield mode and averaged to improve the signal-to-noise ratio. In case of the Ni L-edge, a spectrum of the pristine Ag(111) surface was used for a background correction. In this procedure, the background spectrum was interpolated by a smoothing spline; afterwards, the measured spectra were divided by the spline function.

Structural optimization was carried out with Gaussian09 C.01[48] using the PBE functional[49] and the def2-TZVPP[50] basis set as a part of the density functional theory (DFT) calculations. The "tight" convergence criteria were applied in this regard. Densities of states (DOS) were calculated using the PBE0[51] hybrid functional. Atomic contributions of molecular orbitals were obtained based on the Mulliken population analysis using GaussSum 3.0.[52] For simulations of NEXAFS spectra, the Slater transition potential method[53,54] implemented in the Amsterdam Density Functional (ADF) program package[55] version 2016.106 and the PBE[49] functional were used. Hence, the structures were reoptimized (gridsize m4) including the D3BJ dispersion correction[56] with the def2-TZVPP[50] basis set using Turbomole 7.1. For the simulation itself, the TZ2P[57] basis set was used for all elements except Ni to which the larger, even-tempered ET-QZ3P-3DIFFUSE[58] basis set was supplied for a more detailed description of the core electronic structure. To reproduce the shape of the spectrum, a Gaussian broadening (FWHM = 0.8 eV) was applied on the calculated transitions. The binding situation was further analyzed with the help of the energy decomposition analysis[59–61] (EDA) in combination with the natural orbitals for chemical valence theory[62] (EDA-NOCV) using ADF version 2018.105 and the PBE[49] functional in combination with the TZ2P[57] basis set.

Results and Discussion

Information about the oxidation state of nickel in its complexes was obtained from the position and shape of the Ni 2p XPS signals shown in Fig. 2. To confirm the feasibility of the in situ metalation method,[33–46] we use a film of directly vapor-deposited NiOEP as a reference, because NiOEP is readily available and its stability is well established.[63] The Ni 2p XPS signal of this NiOEP layer is shown in Fig. 2a. The spectra in Figs. 2b and 2c correspond to films of H_2OEP and H_3HEDMC after their partial metalation with vapor-deposited Ni, resulting in the formation of NiOEP and NiHEDMC, respectively. The fraction of metalated molecules was approximately 10%, as was estimated from the N 1s XP spectra presented in Fig. S1 (available online at stacks.iop.org/JSS/9/061005/mmedia) of the

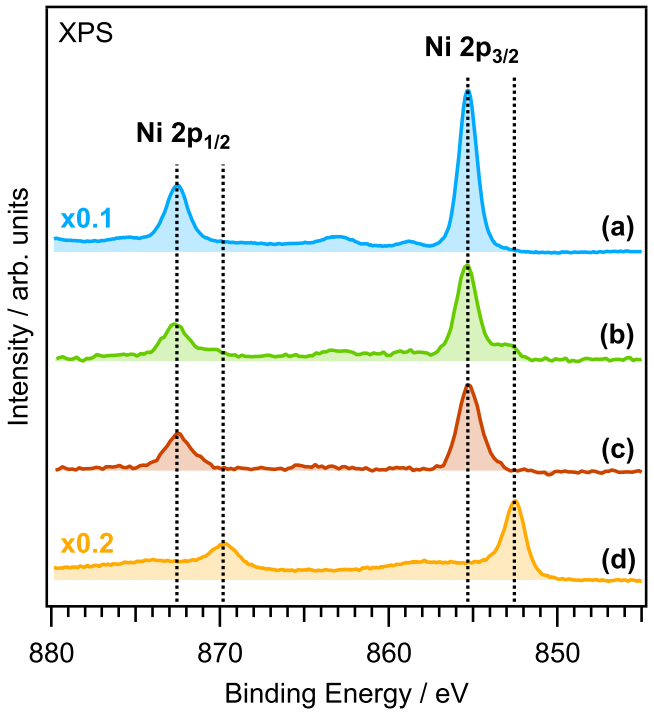

Figure 2. Ni 2p XP spectra of (a) a NiOEP film (reference) and (b), (c) partially Ni metalated films of H_2OEP and H_3HEDMC, resulting in the in situ formation of (b) NiOEP and (c) NiHEDMC. The films have a thickness of 10 monolayers. (d) Ni 2p XP spectrum of Ni directly deposited onto a pristine Ag(111) surface as reference for Ni(0).

supplementary material. Since the XPS signals in the Ni 2p region are element-specific, the unmetalated molecules do not contribute to the spectra and thus do not disturb. The spectrum in Fig. 2d corresponds to Ni directly vapor-deposited onto the clean Ag(111) surface. It serves as a reference for nickel in the zero oxidation state, Ni(0).

Besides some satellite structure, the XP spectrum of the reference NiOEP film (Fig. 2a) shows a narrow Ni $2p_{3/2}$ signal at a binding energy (BE) of 855.3 eV and a Ni $2p_{1/2}$ signal at 872.5 eV. The spectrum has the typical shape and features previously reported for nickel(II) porphyrins.[64,65] The Ni 2p spectrum of the sample prepared by vapor deposition of Ni onto the H_2OEP film (Fig. 2b) is very similar to the NiOEP reference spectrum, indicating successful in situ metalation and formation of NiOEP. The additional shoulders visible at the at low-BE side of the Ni $2p_{3/2}$ and Ni $2p_{1/2}$ signals in Fig. 2b are attributed to small amounts of residual unreacted Ni(0). (Note that these shoulders are shifted towards higher BEs, compared to the Ni(0) reference spectrum in Fig. 2d, due to a less effective core-hole screening in the organic film.)

The spectrum of the partially metalated H_3HEDMC film in Fig. 2c is very similar to the spectrum of NiOEP. In particular, the NiHEDMC spectrum shows a narrow Ni $2p_{3/2}$ signal at 855.2 eV and Ni $2p_{1/2}$ signal at 872.5 eV. These BEs are almost identical to those found for NiOEP. It can therefore be concluded that the Ni ions in NiOEP and NiHEDMC have very similar oxidation states and partial charges. In addition, both spectra lack multiplicity in the Ni 2p region apart from the spin–orbit splitting. Therefore, they support earlier reports[30] that the central nickel atom in corrole complexes is best described as a divalent cation in a low-spin d^8 electron configuration.[66] As a consequence of the formally trianionic nature of the corrole ligand and a divalent central atom, the ligand must bear an unpaired electron. Hence, the studied complex NiHEDMC can be described by the molecular formula shown in Fig. 3b with a delocalized π-radical. This feature represents an important difference between nickel complexes of porphyrin and corrole. Our DFT calculations of the gas-phase structure of NiHEDMC are consistent with these experimental findings. The spin density shows that the unpaired electron is mainly located in a ligand orbital (Fig. 3c). Due to a minor mixing of the singly occupied molecular orbital (SOMO) of the ligand with a d_π orbital of the central metal atom, a small part of the spin-density remains located at the metal center.

Before we turn to the electronic structure in more detail, we briefly discuss the molecular geometry to obtain insight into the structural consequences of the corrole ring contraction. We have analyzed the calculated gas-phase structures of NiOEP and NiHEDMC along with the structures of complexes of the parent ligands, nickel(II) porphine (NiP) and nickel(II) corrole (NiC). In this way, influences of the ring contraction and the peripheral alkyl substituents can be identified and discriminated. In the case of NiOEP, two different minimum-energy structures with almost equal energies were obtained; one is a planar conformer and the other has a strongly out-of-plane distorted ruffled macrocycle. While the ruffled conformer is lower in energy and discussed here in detail, the planar conformer is described in the supplementary material. The cavity size of the macrocycle filled by the nickel ion can be estimated by the lengths of the Ni−N bonds. For NiOEP and NiP, the Ni−N bond lengths are very similar with 1.955 Å and 1.957 Å, respectively (see also Table SI). In comparison, the corrole ligands leave less space for the central nickel atom; the bond lengths range from 1.842 Å to 1.878 Å (see Table SI). (The variation of the bond lengths in the case of the corroles is due to their lower symmetry, compared to the porphyrins.) Unlike corroles, the porphyrin systems undergo substantial out-of-plane distortion to compensate the size mismatch between cavity and central atom. This is a common behavior of porphyrin complexes and was previously reported.[67] The deformation manifests in a so-called ruffling of the macrocycle. In the course of this, the *meso* carbon atoms (i.e., the methine bridges) are displaced alternately above and below the mean plane of the molecule.[16] The distinct ruffling deformation of NiOEP and NiP, compared to the almost planar form of the corrole systems, can be seen in Fig. 4. According to the optimized gas-phase structures, the

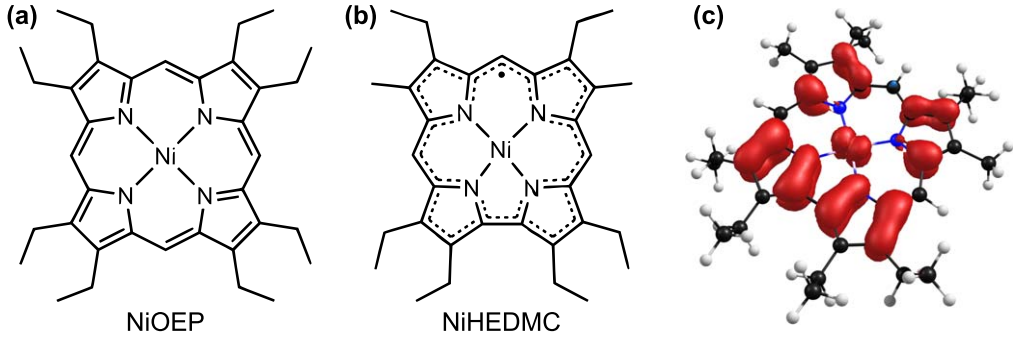

Figure 3. Molecular formulas of the nickel(II) complexes (a) NiOEP and (b) NiHEDMC (as delocalized π-radical). This formulation is consistent with the spin-density (iso surface value = 0.0015) obtained from DFT calculations (PBE/def2-TZVPP) as shown in (c).

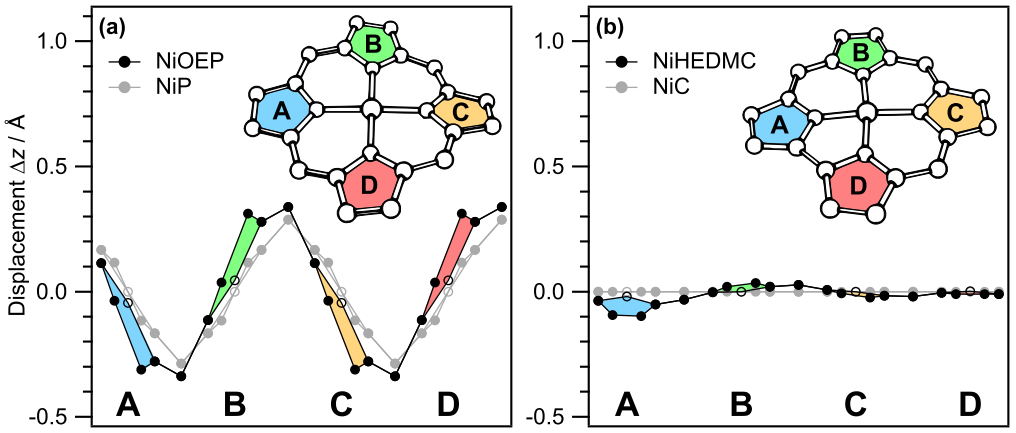

Figure 4. Out-of-plane displacement Δz in Å of the different atoms for (a) NiOEP and NiP and (b) NiC and NiHEDMC. Optimized gas-phase structures (PBE/def2-TZVPP) of NiOEP and NiHEDMC are shown with numbering of the individual pyrrole units (A, B, C, D). Hydrogen atoms and alkyl substituents are omitted for clarity. Δz is given as deviations from the mean plane defined by the average displacement of all atoms.

alkyl substituents have only little impact on the deformation. In conclusion, even when the OEP ligand adopts a strongly ruffled conformation, its cavity remains larger compared to the HEDMC ligand, as indicated by the Ni−N bond lengths.

In the following, we analyze the effects of the ring contraction on the electronic structure. The valence electronic structure in the occupied range was probed using UPS. In Fig. 5, we compare the UP spectra of the nickel complexes with those of the free ligands. This approach allows us to pinpoint the changes in the valence region of the two different ligands upon metalation. To obtain films with higher fractions of the metal complexes while still avoiding unreacted Ni(0), a different layer-by-layer metalation procedure was applied, as described in the supplementary material. Fig. 5 shows valence spectra of H_2OEP and NiOEP (Fig. 5a) and of H_3HEDMC and NiHEDMC (Fig. 5e). In addition, the corresponding difference spectra (nickel complex minus free-base ligand) are presented (Figs. 5b, 5f). For comparison of the experimental spectra

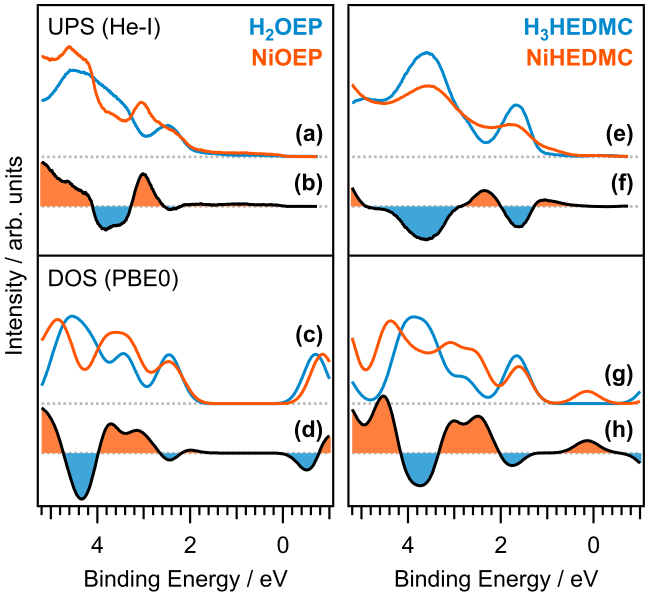

Figure 5. Experimental and calculated valence spectra of the free ligands (blue lines) and the corresponding nickel complexes (orange lines). Experimental photoelectron spectra of (a) H_2OEP and NiOEP, (e) H_3HEDMC and NiHEDMC. (b), (f) Difference spectra (Ni complex minus free ligand). (c), (g) Corresponding calculated DOS (PBE0/def2-TZVPP) and (d), (h) differences in the same color code. For the open shell system NiHEDMC, the two spin channels are summed up. The calculated DOS is aligned to the experimental HOMO energy.

with DFT results, Gaussian broadening (FWHM = 0.6 eV) was applied to the calculated molecular orbital eigenvalues. Because the latter are referenced to the vacuum energy level, which cannot be measured experimentally, the calculated eigenvalues were aligned to the experimental BE of the highest occupied molecular orbital (HOMO). The density of states (DOS) obtained in this way (Figs. 5c, 5g) agrees reasonably well with the experimental spectra considering the limitations of the used method (which includes the initial-state approximation and neglects influences of cross section effects). Looking at the highest occupied states, distinct differences between the experimental spectra of the porphyrin and corrole derivatives upon metalation can be seen. Upon formation of NiOEP, the BE range around 2.3 eV shows almost no changes, while the corrole ligand system shows a peak around 1.6 eV that decreases significantly upon metalation. This peak can be attributed to the HOMO and the SOMO of H_3HEDMC and NiHEDMC, respectively. The decreased peak intensity is a further indication that the metalation product NiHEDMC is a π-radical with one singly occupied ligand orbital. Besides these differences, changes in the electronic structure below the highest occupied states are visible in both ligand systems.

Figure 6 shows the calculated total DOS for both complexes along with the projected densities of states of the nickel atoms (Ni-PDOS). All energies are given as BE and thus aligned to the experimental HOMO energy. Comparison between the total DOS and the Ni-PDOS allows to distinguish between contributions from the ligand and the metal center. Typically, the valence region of porphyrins comprises two sets of mostly degenerate ligand orbitals representing the frontier orbitals.[68] This structure also appears in NiOEP (Fig. 6a), which has two occupied ligand orbitals (with BEs of +2.6 eV and +2.3 eV) and two degenerate unoccupied orbitals (−0.9 eV), resulting in a HOMO-LUMO gap of 3.2 eV. The valence region of NiHEDMC differs from this structure. Here, a singly occupied molecular orbital (SOMO) appears at +1.6 eV. The corresponding singly unoccupied molecular orbital with opposite spin (SUMO) is found at +0.1 eV resulting in a small SOMO −SUMO separation of 1.5 eV. Despite a general shift of the orbital energies to lower BE in case of NiHEDMC, the electronic structure is similar in both complexes; especially the electronic structure of the central atom is similar in both complexes. However, one important feature is the decisive difference for the nickel electronic structure in the unoccupied states. NiOEP has an unoccupied orbital at −1.9 eV BE with a high nickel 3d atomic orbital character. This orbital can be described as a σ^* state formed by the antibonding combination of the nickel $3d_{x2-y2}$ atomic orbital and a ligand orbital. In contrast to this, the corresponding antibonding σ^* orbital of NiHEDMC has a BE of −3.3 eV. The stronger destabilization of the antibonding state in the corrole complex may result from a better

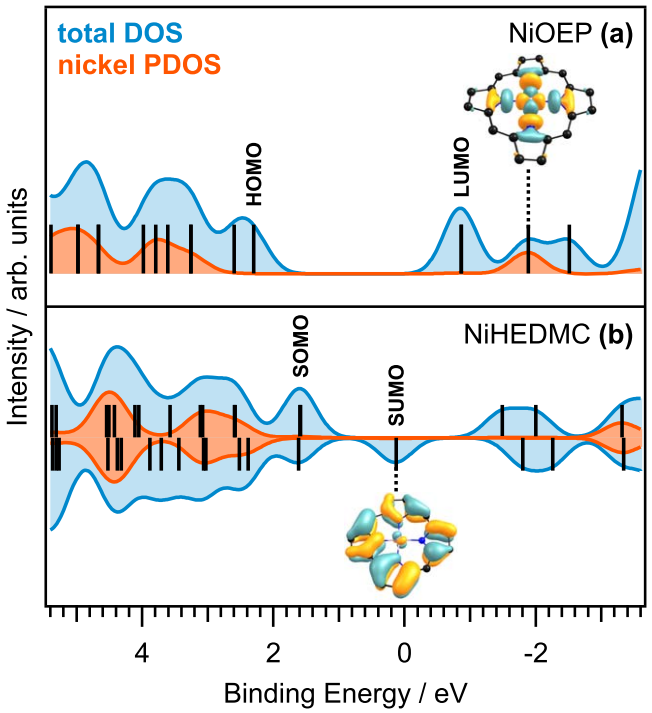

Figure 6. Calculated total DOS (PBE/def2-TZVPP, blue), Ni-PDOS (orange) plotted against the BE for (a) NiOEP and (b) NiHEDMC. The black bars indicate the negative energies of the corresponding orbital eigenvalues. Gaussian broadening (FWHM = 0.6 eV) was applied to the calculated molecular orbital eigenvalues and the Ni atomic orbital contributions to obtain the blue and orange curves, respectively. The DOS and the negative orbital eigenvalues are aligned to the experimental HOMO energy. Visualizations (iso surface value = 0.03) are shown for selected orbitals. Hydrogen atoms and alkyl substituents are omitted for clarity.

overlap of the Ni $3d_{x2-y2}$ atomic orbital with the ligand orbital due to the reduced Ni−N bond length.

NEXAFS spectroscopy provides information about the unoccupied valence states and, thus, was used to verify the calculated electronic structure. Figure 7 shows Ni L-edge absorption spectra of (a) NiOEP and (b) NiHEDMC as well as (c) a Ni(0) reference. In the case of NiOEP, the main transitions appear at 853.4 eV (L_3) and 870.3 eV (L_2), which can be assigned to the transitions from the Ni $2p_{3/2}$ and Ni $2p_{1/2}$ core levels, respectively, to the aforementioned σ^* bond type molecular orbital. The spectrum of NiHEDMC has a similar shape with main transitions at 854.0 eV and 870.9 eV, i.e., the spectrum is shifted to higher photon energies by 0.6 eV relative to the spectrum of NiOEP.

According to a recent NEXAFS study of a nickel porphyrin based molecular spin-state switch,[20] the Ni L-edge of the nickel low-spin d^8 state is characterized by only one main transition, while the corresponding high-spin state shows a double peak structure.[20] Thus, our NEXAFS spectra clearly indicate that nickel has a low-spin d^8 electron configuration in both complexes. The experimental results are corroborated by DFT calculations for the parent molecules NiP and NiC (Figs. 7d, 7e). With the used method (see the computational details), the spin–orbit splitting of the core level is not included within the calculations. Therefore, the simulation does not show separate L_3- and L_2-edges. The calculation supports the assignment of the main transition peak (see visualized orbital in Figs. 7d, 7e). The absolute energy values, the overall shape and the trend are well described by the used method: NiP exhibits a significantly lower excitation energy for the main transition than NiC. Apart from that, all other transitions have only minor contributions to the simulated spectra for both complexes.

These findings clearly support the +2 oxidation state with a low-spin d^8 configuration for the central nickel atom in both complexes.

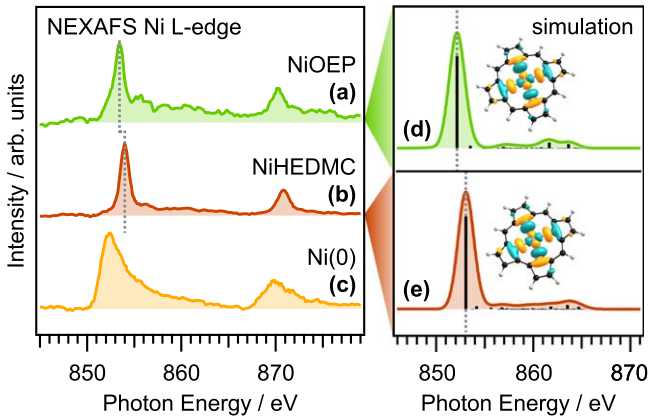

Figure 7. Ni L-edge NEXAFS spectra of (a) NiOEP, (b) NiHEDMC, and (c) Ni on Ag(111). The Ni complexes were prepared by partial in situ metalation of films of the ligands. (d), (e) Simulated spectra of the complexes of the parent macrocycles NiP and NiC. The main transition peak can be assigned to an excitation into the visualized unoccupied orbital (iso surface value = 0.03). The solid lines in the simulation indicate the discrete transition energies.

This means that the stable nickel(II) state forces the corrole ligand to be formally oxidized bearing a π-radical character. Although the former aromatic system of the ligand is lost upon metalation, the reduced aromatic stabilization appears to be compensated by the increased stability of the central atom. As a result of the unpaired electron, nickel corroles are expected to be reduced easily, forming anionic species, in which the aromatic character is reestablished. Nevertheless, an oxidation of the central atom is rather not expected. In contrast to this, reduction of the central atom in nickel porphyrins is known from literature, e.g., in solution[69–71] or in the adsorbed state due to charge transfer from Cu(110) or Cu(100) surfaces to nickel(II) tetraphenylporphyrin.[72,73] Our results show how the reactivity (i.e., ligand vs central atom reduction) can be controlled by varying the ligand structure.

To quantify the different contributions to the chemical bond between the central atom and the ligand, we performed an in-depth bonding analysis. This analysis provides further insight into the influence of the porphyrinoid ring contraction on the nickel−ligand bond. In the framework of an energy decomposition analysis (EDA),[60] the complexes are divided into two fragments along the bond(s) under investigation. This enables the decomposition of the interaction between these fragments in different energy terms. Therefore, the complexes of the parent macrocycles NiP and NiC are divided into two fragments that are as close to the electronic structure the fragments have in the complex as possible. A similar procedure has previously been applied to five- and six-coordinate high-spin iron(III) porphyrin complexes.[74] Here, we omit the peripheral substituents and use the parent molecules NiP (D_{2h}) and NiC (C_{2v}) instead of the experimentally studied substituted systems, because their higher symmetry enables a clearer designation of bonding character to the interactions. In the chosen approach, the complexes were split into a nickel(II) fragment and the corresponding dianionic ligand fragment. In the case of the corrole, the dianionic ligand fragment is a radical bearing an unpaired electron. Table I gives an overview of the individual energy terms obtained within the EDA. Note that negative energies indicate stabilizing interactions, while positive energies indicate repulsive interactions. A detailed description and analysis of these energy terms is given in the supplementary material. Briefly, our findings reveal that the overall Ni-ligand bond is stronger in NiC than in NiP. (In the following, all energies are given in kJ mol^{-1}.) As can be seen in Table I, the overall bonding energy ΔE_{bond} of NiC (−3378) is more negative than that of NiP (−3315). This difference is largely due to an increased interaction energy ΔE_{int}, which comprises attractive (electrostatic ΔE_{elstat} and orbital ΔE_{orb}) and repulsive contributions

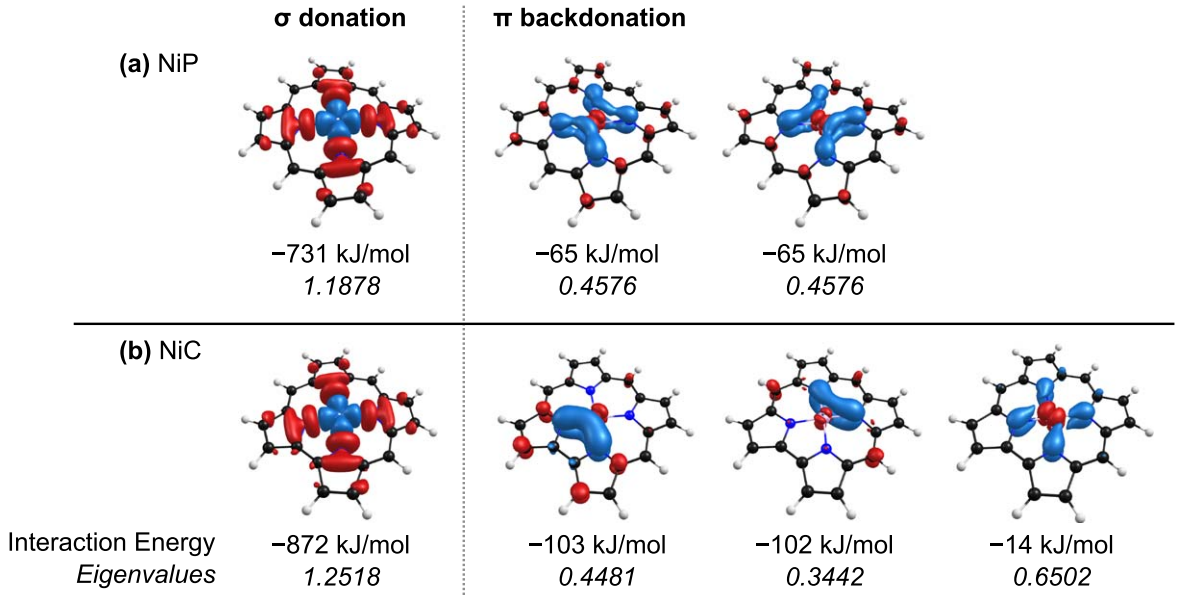

Figure 8. Selected NOCV deformation densities $\Delta\rho_i$ (iso surface value = 0.03) for (a) NiP and (b) NiC. Blue regions show charge accumulation and red regions charge depletion.

Table I. Results of the energy decomposition analysis (EDA) for the nickel complexes of the parent macrocycles NiP and NiC. Energies in kJ mol^{-1}; bond length *d* in Å.

	NiP (D_{2h})		NiC (C_{2v})	
ΔE_{int}	−3701		−3798	
ΔE_{Pauli}	+720		+1071	
ΔE_{elstat} [a)]	−2727	(62%)	−2946	(61%)
ΔE_{orb} [a)]	−1694	(38%)	−1923	(39%)
$\Delta E(\sigma$ donation) [b)]	−1055	(62%)	−1203	(61%)
$\Delta E(\pi$ backdonation) [b)]	−130	(8%)	−219	(11%)
ΔE(polarization) [b)]	−273	(16%)	−233	(12%)
ΔE(rest) [b)]	−237	(14%)	−308	(16%)
ΔE_{prep}	+386		+421	
ΔE_{deform} [c)]	+70	(18%)	+59	(14%)
ΔE_{exc} [c)]	+316	(82%)	+362	(86%)
ΔE_{bond}	−3315		−3378	
d(Ni−N)	1.957		1.842, 1.872	

a) Values in parentheses give the percentage contribution to the total attractive interactions $\Delta E_{elstat} + \Delta E_{orb}$. b) Values in parentheses give the percentage contribution to the orbital interactions ΔE_{orb}. c) Values in parentheses give the percentage contribution to the preparation energy ΔE_{prep}.

(Pauli repulsion ΔE_{Pauli}). The Pauli repulsion is stronger in NiC than in NiP (+1071 vs +720), but this is overcompensated by the stronger electrostatic (−2946 vs −2727) and orbital (−1923 vs −1694) attraction in the corrole complex. As a result, NiC has the more negative interaction energy (−3798 vs −3701). The stronger Pauli repulsion and the more attractive ΔE_{elstat} as well as the increased ΔE_{orb} in the case of NiC can be attributed to the shorter Ni−N bond distances and, thus, can be seen as a direct consequence of the smaller corrole cavity. A further partitioning of the orbital interactions in contributions of individual symmetry terms is given in the supplementary material.

The combination of the EDA with the natural orbital for chemical valence theory (EDA-NOCV)[62] enables further partitioning and interpretation of the orbital interaction ΔE_{orb}. ΔE_{orb} is divided into contributions of pairwise interactions between an orbital of the central atom and a ligand orbital of corresponding symmetry, referred to as deformation densities $\Delta\rho_i$. The deformation densities for each interaction can be visualized, which allows a classification of the interactions in categories by visual inspection. The EDA-NOCV also provides, as quantitative results, the corresponding energies ΔE_i for each interaction and the eigenvalues v_i that give an indication on the amount of charge flow in number of electrons. For a more detailed description of the method, the reader is referred to the supplementary material and the literature.[60,62]

Figure 8 shows selected deformation densities, which represent the most tangible interactions. For all of these, σ donation and π backdonations, the interactions are stronger in the corrole complex than in the porphyrin complex. The larger amount of charge that is redistributed by the formation of the Ni−N bond indicates a stronger bond to the central atom in nickel corroles. This is in line with the increased overall ΔE_{orb} term for the corrole complex. The nature of this bond influences the electronic structure of the nickel center, making the porphyrinoid ring contraction a viable way of tuning the properties of the central atom without changing its formal oxidation state.

Conclusions

The influence of ring contraction on the electronic structure of nickel tetrapyrrole complexes was studied by comparing the nickel corrole NiHEDMC with the nickel porphyrin NiOEP using XPS, UPS, and NEXAFS measurements, in combination with DFT calculations. The Ni 2p XP and Ni L-edge NEXAFS spectra support previous findings that both complexes contain low-spin d^8 Ni(II) cations. In the case of NiHEDMC, the combination of a trianionic ligand with the divalent central atom leads to a ligand π-radical, as was confirmed by computations. The calculated SOMO-related spin density is mainly located on the ligand. UPS shows that the HOMO intensity of the free corrole ligand decreases upon metalation with Ni, supporting the radical character of the corrole ligand in NiHEDMC. The valence spectra are in line with the calculated DOS. The Ni-PDOS supports the Ni d^8 electron configuration with one unoccupied Ni 3d type valence orbital, which can be described as the antibonding combination of a ligand orbital with the Ni $3d_{x2-y2}$ forming a Ni−N σ* state. The corresponding state has a much higher energy in NiHEDMC than in NiOEP, in agreement with the NEXAFS data. The Ni L-edges of both complexes have a similar shape with one narrow main feature, which can be assigned to the transition from the Ni 2p level to the aforementioned Ni−N σ* state. In-depth bonding analysis by the EDA-NOCV theory reveals

that Ni-corrole and Ni-porphyrin bonds show the same bonding character. However, the Ni-corrole bond shows larger interaction energy terms throughout, resulting in a higher overall bonding energy. The stronger Ni-N interactions in the corrole are attributed to its shorter Ni−N bonds. Calculations of the gas-phase structures reveal a ruffled porphyrin core in NiOEP, while the corrole core in NiHEDMC is almost planar. The reason for the ruffling of NiOEP lies in the size mismatch between the small Ni(II) cation and the large cavity of the porphyrin. Even with the effective contraction of the porphyrin ligand due to the ruffling, the Ni−N distance in NiOEP is larger than the Ni-N distances in NiHEDMC. Our results show that a seemingly small change of the ligand skeletal structure can lead to substantial changes of the electronic structure and the metal-ligand interaction, even when the formal oxidation number of the metal center remains unchanged.

Acknowledgments

Financial support by the Deutsche Forschungsgemeinschaft (DFG) through the SFB 1083 (223848855-SFB 1083) is gratefully acknowledged. We thank DESY (Hamburg, Germany), a member of the Helmholtz Association HGF, for the provision of experimental facilities. Parts of this research were carried out at PETRA III. Funding for the photoemission spectroscopy instrument ASPHERE at beamline P04 (Contracts 05KS7FK2, 05K10FK1, 05K12FK1, and 05K13FK1 with Kiel University; 05KS7WW1 and 05K10WW2 with Würzburg University) by the Federal Ministry of Education and Research (BMBF) is gratefully acknowledged. We thank HRZ Marburg, Goethe-CSC Frankfurt and HLRS Stuttgart for computational resources.

ORCID

Kai Rossnagel https://orcid.org/0000-0001-5107-0090
Ralf Tonner https://orcid.org/0000-0002-6759-8559
J. Michael Gottfried https://orcid.org/0000-0001-5579-2568

References

1. S. W. Ragsdale, *J. Biol. Chem.*, **284**, 18571 (2009).
2. R. A. Ware and J. Wei, *J. Catal.*, **93**, 100 (1985).
3. P. Schaeffer, R. Ocampo, H. J. Callot, and P. Albrecht, *Nature*, **364**, 133 (1993).
4. W. S. Caughey, R. M. Deal, B. D. McLees, and J. O. Alben, *J. Am. Chem. Soc.*, **84**, 1735 (1962).
5. D. Kim, C. Kirmaier, and D. Holten, *Chem. Phys.*, **75**, 305 (1983).
6. D. Kim and D. Holten, *Chem. Phys. Lett.*, **98**, 584 (1983).
7. L. X. Chen, W. J. H. Jäger, G. Jennings, D. J. Gosztola, A. Munkholm, and J. P. Hessler, *Science*, **292**, 262 (2001).
8. S. Thies, C. Bornholdt, F. Köhler, F. D. Sönnichsen, C. Näther, F. Tuczek, and R. Herges, *Chem. Eur. J.*, **16**, 10074 (2010).
9. M. K. Peters and R. Herges, *Inorg. Chem.*, **57**, 3177 (2018).
10. A. G. Martynov, E. A. Safonova, A. Y. Tsivadze, and Y. G. Gorbunova, *Coordin. Chem. Rev.*, **387**, 325 (2019).
11. E. F. Meyer, *Acta Crystall., B*, **28**, 2162 (1972).
12. R. G. Alden, B. A. Crawford, R. Doolen, M. R. Ondrias, and J. A. Shelnutt, *J. Am. Chem. Soc.*, **111**, 2070 (1989).
13. X. Y. Li, R. S. Czernuszewicz, J. R. Kincaid, and T. G. Spiro, *J. Am. Chem. Soc.*, **111**, 7012 (1989).
14. J. A. Shelnutt, C. J. Medforth, M. D. Berber, K. M. Barkigia, and K. M. Smith, *J. Am. Chem. Soc.*, **113**, 4077 (1991).
15. K. K. Anderson, J. D. Hobbs, L. Luo, K. D. Stanley, J. M. E. Quirke, and J. A. Shelnutt, *J. Am. Chem. Soc.*, **115**, 12346 (1993).
16. W. Jentzen et al., *J. Am. Chem. Soc.*, **117**, 11085 (1995).
17. C. M. Drain et al., *J. Am. Chem. Soc.*, **120**, 3781 (1998).
18. J. S. Evans and R. L. Musselman, *Inorg. Chem.*, **43**, 5613 (2004).
19. J. L. Hoard, *Ann. N. Y. Acad. Sci.*, **206**, 18 (1973).
20. A. Köbke et al., *Nat. Nanotechnol.*, **15**, 18 (2020).
21. S. Nardis, D. Monti, and R. Paolesse, *Mini-Rev. Org. Chem.*, **2**, 355 (2005).
22. J. H. Palmer, *Struct. Bond.*, **142**, 49 (2012).
23. A. Ghosh, *Chem. Rev.*, **117**, 3798 (2017).
24. S. Nardis, F. Mandoj, M. Stefanelli, and R. Paolesse, *Coordin. Chem. Rev.*, **388**, 360 (2019).
25. I. Aviv and Z. Gross, *Chem. Commun.*, 1987 (2007).
26. A. W. Johnson and I. T. Kay, *J. Chem. Soc.*, 1620 (1965).
27. R. Grigg, A. W. Johnson, and G. Shelton, *Chem. Commun.*, 1151 (1968).
28. R. Grigg, A. W. Johnson, and G. Shelton, *Liebigs Ann. Chem.*, **746**, 32 (1971).
29. Y. Murakami, Y. Matsuda, K. Sakata, S. Yamada, Y. Tanaka, and Y. Aoyama, *Bull. Chem. Soc. Jpn.*, **54**, 163 (1981).
30. S. Will, J. Lex, E. Vogel, H. Schmickler, J. P. Gisselbrecht, C. Haubtmann, M. Bernard, and M. Gross, *Angew. Chem. Int. Ed.*, **36**, 357 (1997).
31. A. Ghosh, T. Wondimagegn, and A. B. J. Parusel, *J. Am. Chem. Soc.*, **122**, 5100 (2000).
32. B. van Oort, E. Tangen, and A. Ghosh, *Eur. J. Inorg. Chem.*, 2442 (2004).
33. T. E. Shubina, H. Marbach, K. Flechtner, A. Kretschmann, N. Jux, F. Buchner, H. P. Steinruck, T. Clark, and J. M. Gottfried, *J. Am. Chem. Soc.*, **129**, 9476 (2007).
34. M. Schmid et al., *J. Phys. Chem. C*, **122**, 10392 (2018).
35. K. Diller, A. C. Papageorgiou, F. Klappenberger, F. Allegretti, J. V. Barth, and W. Auwärter, *Chem. Soc. Rev.*, **45**, 1629 (2016).
36. H. Marbach, *Acc. Chem. Res.*, **48**, 2649 (2015).
37. J. M. Gottfried, *Surf. Sci. Rep.*, **70**, 259 (2015).
38. J. M. Gottfried, K. Flechtner, A. Kretschmann, T. Lukasczyk, and H. P. Steinrück, *J. Am. Chem. Soc.*, **128**, 5644 (2006).
39. Y. Bai, F. Buchner, M. T. Wendahl, I. Kellner, A. Bayer, H. P. Steinrück, H. Marbach, and J. M. Gottfried, *J. Phys. Chem. C*, **112**, 6087 (2008).
40. C. C. Wang, Q. T. Fan, S. W. Hu, H. X. Ju, X. F. Feng, Y. Han, H. B. Pan, J. F. Zhu, and J. M. Gottfried, *Chem. Commun.*, **50**, 8291 (2014).
41. T. Lukasczyk, K. Flechtner, L. R. Merte, N. Jux, F. Maier, J. M. Gottfried, and H. P. Steinruck, *J. Phys. Chem. C*, **111**, 3090 (2007).
42. M. Chen, X. F. Feng, L. Zhang, H. X. Ju, Q. Xu, J. F. Zhu, J. M. Gottfried, K. Ibrahim, H. J. Qian, and J. O. Wang, *J. Phys. Chem. C*, **114**, 9908 (2010).
43. A. Goldoni, C. A. Pignedoli, G. Di Santo, C. Castellarin-Cudia, E. Magnano, F. Bondino, A. Verdini, and D. Passerone, *ACS Nano*, **6**, 10800 (2012).
44. S. Ditze, M. Röckert, F. Buchner, E. Zillner, M. Stark, H. P. Steinrück, and H. Marbach, *Nanotechnology*, **24**, 115305 (2013).
45. M. Schmid, S. R. Kachel, B. P. Klein, N. Bock, P. Müller, R. Riedel, N. Hampp, and J. M. Gottfried, *J. Phys. Condens. Matter*, **31**, 094002 (2019).
46. M. Chen, H. Zhou, B. P. Klein, M. Zugermeier, C. K. Krug, H. J. Drescher, M. Gorgoi, M. Schmid, and J. M. Gottfried, *Phys. Chem. Chem. Phys.*, **18**, 30643 (2016).
47. J. Viefhaus, F. Scholz, S. Deinert, L. Glaser, M. Ilchen, J. Seltmann, P. Walter, and F. Siewert, *Nucl. Instrum. Meth. A*, **710**, 151 (2013).
48. J. R. M. J. Frisch et al., *Gaussian 09 Revision C.01* (Gaussian Inc, Wallingford CT) (2009).
49. J. P. Perdew, K. Burke, and M. Ernzerhof, *Phys. Rev. Lett.*, **77**, 3865 (1996).
50. F. Weigend and R. Ahlrichs, *Phys. Chem. Chem. Phys.*, **7**, 3297 (2005).
51. C. Adamo and V. Barone, *J. Chem. Phys.*, **110**, 6158 (1999).
52. N. M. O'Boyle, A. L. Tenderholt, and K. M. Langner, *J. Comput. Chem.*, **29**, 839 (2008).
53. R. De Francesco, M. Stener, and G. Fronzoni, *J. Phys. Chem. A*, **116**, 2885 (2012).
54. G. Fronzoni, G. Balducci, R. De Francesco, M. Romeo, and M. Stener, *J. Phys. Chem. C*, **116**, 18910 (2012).
55. G. te Velde, F. M. Bickelhaupt, E. J. Baerends, C. Fonseca Guerra, S. J. A. van Gisbergen, J. G. Snijders, and T. Ziegler, *J. Comput. Chem.*, **22**, 931 (2001).
56. S. Grimme, S. Ehrlich, and L. Goerigk, *J. Comput. Chem.*, **32**, 1456 (2011).
57. E. van Lenthe and E. J. Baerends, *J. Comput. Chem.*, **24**, 1142 (2003).
58. D. P. Chong, E. van Lenthe, S. van Gisbergen, and E. J. Baerends, *J. Comput. Chem.*, **25**, 1030 (2004).
59. T. Ziegler and A. Rauk, *Theoret. Chim. Acta*, **46**, 1 (1977).
60. L. Zhao, M. von Hopffgarten, D. M. Andrada, and G. Frenking, *WIREs Comput Mol Sci*, **8**, e1345 (2018).
61. F. M. Bickelhaupt and E. J. Baerends, *Kohn–Sham Density Functional Theory: Predicting and Understanding Chemistry* (Wiley-VCH, Inc, New York) (2000).
62. P. M. Mitoraj, A. Michalak, and T. Ziegler, *J. Chem. Theory Comput.*, **5**, 962 (2009).
63. L. Scudiero, D. E. Barlow, and K. W. Hipps, *J. Phys. Chem. B*, **106**, 996 (2002).
64. P. S. Johnson, J. M. Garcia-Lastra, C. K. Kennedy, N. J. Jersett, I. Boukahil, F. J. Himpsel, and P. L. Cook, *J. Chem. Phys.*, **140**, 114706 (2014).
65. S. A. Krasnikov, A. B. Preobrajenski, N. N. Sergeeva, M. M. Brzhezinskaya, M. A. Nesterov, A. A. Cafolla, M. O. Senge, and A. S. Vinogradov, *Chem. Phys.*, **332**, 318 (2007).
66. G. I. Svirskiy, N. N. Sergeeva, S. A. Krasnikov, N. A. Vinogradov, Y. N. Sergeeva, A. A. Cafolla, A. B. Preobrajenski, and A. S. Vinogradov, *Phys. Solid State*, **59**, 368 (2017).
67. J. Conradie and A. Ghosh, *ACS Omega*, **2**, 6708 (2017).
68. M. Gouterman, G. H. Wagnière, and L. C. Snyder, *J. Mol. Spectrosc.*, **11**, 108 (1963).
69. D. Lexa, M. Momenteau, J. Mispelter, and J. M. Savéant, *Inorg. Chem.*, **28**, 30 (1989).
70. G. S. Nahor, P. Neta, P. Hambright, L. R. Robinson, and A. Harriman, *J. Phys. Chem.*, **94**, 6659 (1990).
71. Y. Z. Han, H. Y. Fang, H. Z. Jing, H. L. Sun, H. T. Lei, W. Z. Lai, and R. Cao, *Angew. Chem. Int. Ed.*, **55**, 5457 (2016).
72. G. Zamborlini et al., *Nat. Commun.*, **8**, 335 (2017).
73. G. Zamborlini, M. Jugovac, A. Cossaro, A. Verdini, L. Floreano, D. Luftner, P. Puschnig, V. Feyer, and C. M. Schneider, *Chem. Commun.*, **54**, 13423 (2018).
74. R.-J. Cheng, P.-Y. Chen, T. Lovell, T. Liu, L. Noodleman, and D. A. Case, *J. Am. Chem. Soc.*, **125**, 6774 (2003).